Measurement of gluon fusion and vector boson fusion Higgs boson production cross-sections in the $H \rightarrow WW^* \rightarrow e\nu\mu\nu$ decay channel in pp collisions at $\sqrt{s} = 13$ TeV with the ATLAS detector

The ATLAS Collaboration

The Higgs boson production cross-sections in proton-proton collisions are measured in the $H \rightarrow WW^* \rightarrow e\nu\mu\nu$ decay channel. The proton-proton collision data were produced at the Large Hadron Collider at a centre-of-mass energy of 13 TeV and recorded by the ATLAS detector in 2015 and 2016, corresponding to an integrated luminosity of 36.1 fb^{-1}. The gluon fusion and vector boson fusion cross-sections times the $H \rightarrow WW^*$ branching ratio are measured to be $12.6^{+1.3}_{-1.2}$(stat.)$^{+1.9}_{-1.8}$(sys.) pb and $0.50^{+0.24}_{-0.23}$(stat.) $\pm$ 0.18(sys.) pb, respectively, in agreement with the Standard Model predictions.

This note presents a measurement of the Higgs boson production via gluon fusion (ggF) and vector boson fusion (VBF) observed through the decay $H \rightarrow WW^* \rightarrow e\nu\mu\nu$ using 36.1 fb^{-1} of pp collisions at a centre-of-mass energy of 13 TeV recorded by the ATLAS detector. The measured cross-sections probe the Higgs boson couplings to heavy bosons and to gluons via loops of heavy particles.

ATLAS is a particle detector designed to achieve nearly a full coverage in solid angle [1]. It consists of an inner tracking detector surrounded by a thin superconducting solenoid, electromagnetic and hadronic calorimeters, and a muon spectrometer incorporating three large superconducting toroidal magnets. The inner tracking detector (ID) is inside a 2 T magnetic field and is designed to measure charged-particle trajectories up to a pseudorapidity of $|\eta| = 2.5$. An additional pixel layer was installed for the $\sqrt{s} = 13$ TeV running period [2]. Surrounding the ID are electromagnetic and hadronic calorimeters, which use liquid argon (LAr) and lead, copper absorber for the electromagnetic and endcap ($|\eta| > 1.7$) hadronic calorimeters, and scintillator-tile active material with steel absorber for the central ($|\eta| < 1.7$) hadronic calorimeter. The solid angle coverage is extended to $|\eta| < 4.9$ with forward copper/LAr and tungsten/LAr calorimeter modules. The muon spectrometer comprises separate trigger and high-precision tracking chambers measuring the deflection of muons in a magnetic field generated by a superconducting air-core toroid. A two-level trigger system is used to select events [3].

Several Monte Carlo (MC) simulations are used to compare to data. The Standard Model (SM) Higgs boson production via ggF is simulated at next-to-next-to-leading-order (NNLO) accuracy in QCD and VBF at next-to-leading-order (NLO) accuracy in QCD using the POWHEG-BOX v2 [4–6] with the PDF4LHC15 NNLO or NLO set of parton distribution functions (PDF) [7], respectively. The PYTHIA 8 [8] generator is used for the $H \rightarrow WW^* \rightarrow \ell\nu\ell\nu$ decay ($\ell = e$ or μ, but including contributions from fully-leptonic τ decays) as well as for the parton shower model using the AZNLO tune [9]. The ggF production cross-section is calculated with next-to-next-to-next-to-leading order accuracy in QCD and has NLO electroweak (EW) corrections [10–14]. The full NLO QCD and EW calculations are used with approximate NNLO QCD corrections for the VBF production cross-section [10, 15–17]. The generated Higgs boson events are passed through a GEANT 4 [18] simulation of the ATLAS detector [19] and reconstructed with the same analysis software used for the data. Additional proton–proton interactions (pileup) are included in the simulation for all generated events such that the average number of interactions per bunch crossing reproduces that observed in the data. The inelastic proton–proton collisions were produced using PYTHIA 8 with the A2 parameter set [20] that is tuned to data and the MSTW2008LO PDF set [21]. MC-to-data corrections are applied to the simulated events in order to improve the agreement with data. The MC generators, PDFs, and parton showers used to produce the simulated samples that model the signal and background processes are summarized in Table 1. The precision of the cross-section used for each sample is also reported.

Events are triggered using both single lepton and di-lepton triggers. The transverse momentum (p_{T}) threshold ranges between 24 GeV and 26 GeV for single electron triggers and between 20 GeV and 26 GeV for single muon triggers [3]. Di-lepton triggers require a minimum p_{T} threshold of 17 GeV for electrons and 14 GeV for muons. Electron candidates are reconstructed from energy clusters in the electromagnetic calorimeter with an associated well-reconstructed track [44, 45]. Electrons are required to have $|\eta| < 2.47$, excluding the transition region between the barrel and endcap calorimeters of $1.37 < |\eta| < 1.52$. Muon candidates are selected from tracks reconstructed in the ID matched to tracks reconstructed in the muon spectrometer [46] and are required to have $|\eta| < 2.5$. To reject particles misidentified as leptons, several identification requirements as well as calorimeter and track isolation criteria [46, 47] are applied. The final lepton selection criteria require two different-flavour leptons, the higher-p_{T} (leading) lepton with $p_{\mathrm{T}} > 22$ GeV and the subleading lepton with $p_{\mathrm{T}} > 15$ GeV. At least one of the leptons should correspond

Table 1: MC generators used to generate the matrix-element processes used for the simulation of all signal and background processes. Parton Distribution Functions (PDF), as well as parton shower (PS) software are also summarised. Alternative event generators and configurations used to estimate systematic uncertainties are also shown and placed in parentheses. The column "Precision σ" gives the precision of the cross-section applied to the sample.

Process	Matrix Element (Alternative)	PDF	PS (Alternative)	Precision σ
ggF	POWHEG-BOX v2 NNLOPS [4–6] (MG5_aMC@NLO [22, 23])	PDF4LHC15 NNLO [7]	PYTHIA 8 [8] (HERWIG 7 [24])	N^3LO QCD + NLO EW [10–14]
VBF	POWHEG-BOX v2 (MG5_aMC@NLO)	PDF4LHC15 NLO	PYTHIA 8 (HERWIG 7)	NNLO QCD + NLO EW [10, 15–17]
VH	POWHEG-BOX v2 [25]	PDF4LHC15 NLO	PYTHIA 8	NNLO QCD + NLO EW [26–28]
$qq \rightarrow WW$	SHERPA 2.2.2 [29, 30] (POWHEG-BOX v2, MG5_aMC@NLO)	NNPDF3.0NNLO [31]	SHERPA 2.2.2 [32, 33] (HERWIG++ [24])	NLO [34]
$gg \rightarrow WW$	SHERPA 2.1.1 [34]	CT10 [35]	SHERPA 2.1	NLO [36]
WZ/$V\gamma^*$/ZZ	SHERPA 2.1	CT10	SHERPA 2.1	NLO [34]
Vγ	SHERPA 2.2.2 (MG5_aMC@NLO)	NNPDF3.0NNLO	SHERPA 2.2.2 (CSS variation [32, 37])	NLO [34]
$t\bar{t}$	POWHEG-BOX v2 [38] SHERPA 2.2.1	NNPDF3.0NLO	PYTHIA 8 [39] (HERWIG 7)	NNLO+NNLL [40]
Wt	POWHEG-BOX v1 [41] (MG5_aMC@NLO)	CT10 [35]	PYTHIA 6.428 [42] (HERWIG++)	NLO [41]
Z+jets	SHERPA 2.2.1	NNPDF3.0NNLO	SHERPA 2.2.1	NLO [43]

to a lepton that triggered the recording of the event. In case a di-lepton trigger is solely responsible for the recording of the event, each lepton should be associated to one of the trigger objects. Jets are reconstructed using the anti-k_t algorithm [48] with a radius parameter $R = 0.4$. The four-momenta of jets are corrected for the effects of calorimeter non-compensation, signal losses due to noise threshold effects, energy lost in non-instrumental regions, and contributions from pile-up [49]. Jets are required to have $p_T > 20$ GeV and $|\eta| < 4.5$. A multivariate selection that reduces contamination from pileup [50, 51] is applied to jets with $p_T < 60$ GeV and $|\eta| < 2.4$ utilising calorimeter and tracking information to separate hard-scatter from pile-up jets. For jets with $p_T < 50$ GeV and $|\eta| > 2.5$, jet shapes and topological jet correlations in pile-up interactions are exploited to reduce contamination from pileup. Jets containing b-hadrons (b-jets) with $p_T > 20$ GeV and $|\eta| < 2.5$ are identified using a multivariate technique having as input information from track impact parameters and secondary vertices. The adopted working point provides a nominal 3% light-flavour (u,d,s-quark and gluon) misidentification efficiency and a 32% c-jet misidentification efficiency with an average 85% b-jet tagging efficiency, as estimated from simulated $t\bar{t}$ events in the above-mentioned kinematic region [52]. Removal of overlapping jet and lepton candidates is performed for nearby objects. The vectorial missing transverse momentum (E_T^{miss}) is defined as the negative vector sum of the p_T of all the selected leptons and jets, as well as reconstructed charged particles not associated with these objects, but consistent with originating from the primary pp collision [53]. The missing transverse momentum (E_T^{miss}) is defined as the magnitude of E_T^{miss}. A second definition of missing transverse momentum ($E_T^{miss, track}$) is also used in which tracks associated with jets are used rather than calorimeter-based jets.

Events are classified into one of three categories based on the number of jets with $p_T > 30$ GeV in the event: events with zero jets and events with exactly one jet target the ggF production channel ($N_{jet} = 0$ and $N_{jet} = 1$ category), and events with at least two jets target the VBF production channel ($N_{jet} \geq 2$ VBF category). A b-jet veto is applied in all categories to jets with $p_T > 20$ GeV ($N_{b\text{-jet},(p_T>20 \text{ GeV})}$) to reject background

from top-quark production. The full event selection is summarised in Table 2, where $\Delta\phi(\ell\ell, E_T^{miss})$ is defined as the azimuth angle between $\boldsymbol{E}_T^{miss}$ and the di-lepton system, $p_T^{\ell\ell}$ is the transverse momentum of the di-lepton system, $m_{\ell\ell}$ is the invariant mass of the two leptons, $\Delta\phi_{\ell\ell}$ is the azimuth angle between the two leptons, and $\max\left(m_T^\ell\right)$ is the maximum of $m_T^{\ell_i} = \sqrt{2\,p_T\,(\ell_i)\cdot E_T^{miss}\cdot\left(1 - \cos\Delta\phi\left(\boldsymbol{\ell}_i, \boldsymbol{E}_T^{miss}\right)\right)}$, where ℓ_i can either be the leading or the subleading lepton. The "Outside Lepton Veto" requires the two leptons to reside within the rapidity gap spanned by the two leading jets, and the "Central Jet Veto" rejects events with additional jets with $p_T > 20\,\text{GeV}$ in the rapidity gap of the two leading jets. In the $N_{jet} = 1$ and $N_{jet} \geq 2$ categories the invariant mass of the $\tau\tau$ system ($m_{\tau\tau}$), calculated using the collinear approximation [54], is used to veto background from $Z \to \tau\tau$ production. Signal regions (SRs) are defined in each N_{jet} category after all selection criteria are applied.

In case of the SRs targeting the ggF production mode, the discriminating variable between signal and SM background processes is the transverse mass, defined as $m_T = \sqrt{\left(E_T^{\ell\ell} + E_T^{miss}\right)^2 - \left|\mathbf{p}_T^{\ell\ell} + \boldsymbol{E}_T^{miss}\right|^2}$ where $E_T^{\ell\ell} = \sqrt{|\mathbf{p}_T^{\ell\ell}|^2 + m_{\ell\ell}^2}$ and $\mathbf{p}_T^{\ell\ell}$ is the vector sum of the lepton transverse momenta. For the VBF selection, a boosted decision tree (BDT) [55] is used to enhance discrimination power between the VBF signal and backgrounds, including the ggF process. Kinematic variables of the two leading jets (j) and two leading leptons (ℓ), including invariant masses (m_{jj}, $m_{\ell\ell}$), difference in the two jet rapidities (Δy_{jj}), and difference in the azimuth angles of the two leptons ($\Delta\phi_{\ell\ell}$), are used as inputs to the BDT. Other variables used in the BDT training are: the transverse mass (m_T), the lepton η-centrality ($\sum C_\ell$) which quantifies the positions of the leptons with respect to the leading jets in the pseudorapidity direction, the sum of the invariant masses of all four possible lepton-jet pairs ($\sum_{\ell,j} m_{\ell j}$), and the total transverse momentum (p_T^{tot}) which is defined as the magnitude of the vectorial sum of all the objects in the final state. The variables with the highest ranking in the training, m_{jj} and Δy_{jj}, are shown in Figure 1 after all selection cuts have been applied. All figures in this note use signal and background normalisations as given by the final statistical analysis of all signal and control regions, including changes to statistical and systematic uncertainties (post-fit).

Table 2: Event selection criteria used to define the signal regions in the $H \to WW^* \to e\nu\mu\nu$ analysis.

Category		$N_{jet} = 0$	$N_{jet} = 1$	$N_{jet} \geq 2$, VBF
Preselection		Two isolated, different-flavour, leptons ($\ell = e, \mu$) with opposite charge $p_T^{lead} > 22$ GeV , $p_T^{sublead} > 15$ GeV $m_{\ell\ell} > 10$ GeV	
		$E_T^{miss, track} > 20$ GeV		
Background rejection			$N_{b\text{-jet},\,(p_T > 20\text{ GeV})} = 0$	
		$\Delta\phi(\ell\ell, E_T^{miss}) > \pi/2$ $p_T^{\ell\ell} > 30$ GeV	$\max\left(m_T^\ell\right) > 50$ GeV	$m_{\tau\tau} < m_Z - 25$ GeV
$H \to WW^* \to e\nu\mu\nu$ topology		\multicolumn{2}{c}{$m_{\ell\ell} < 55$ GeV $\Delta\phi_{\ell\ell} < 1.8$}	Central Jet Veto Outside Lepton Veto
Discriminant Variable BDT input variables		\multicolumn{2}{c}{m_T}	BDT $m_{jj}, \Delta y_{jj}, m_{\ell\ell}, \Delta\phi_{\ell\ell}, m_T, \sum C_\ell, \sum_{\ell,j} m_{\ell j}, p_T^{tot}$

The background contamination in the SRs comes from various processes: non-resonant WW, top-quark pair ($t\bar{t}$) and single-top-quark (Wt), diboson (WZ, ZZ, $W\gamma$ and $W\gamma^*$) and Drell-Yan (mainly $Z \to \tau\tau$) production. Another background contribution arises from the misidentified leptons stemming from the W+jets and QCD multi-jet production. Dedicated control regions (CRs) are used to normalise the
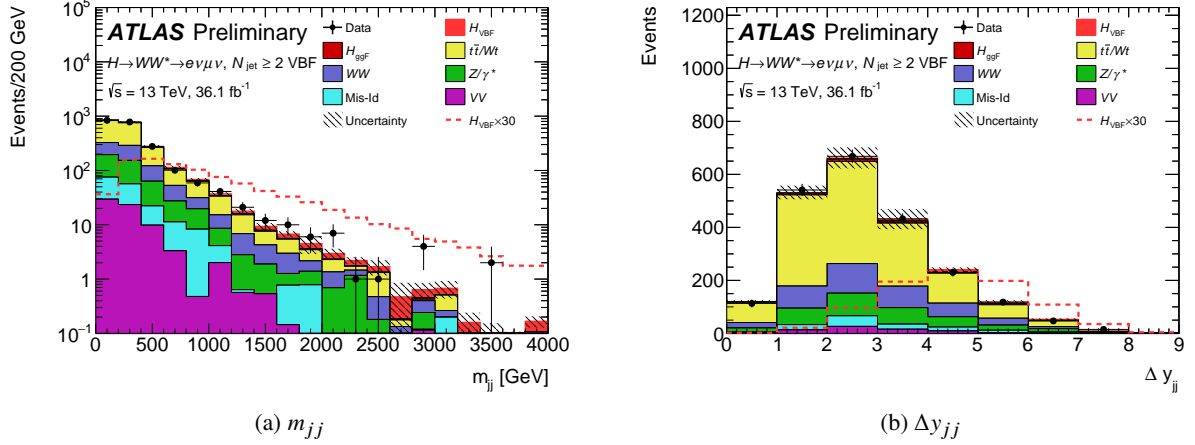
Figure 1: Post-fit m_{jj} and Δy_{jj} distributions with signal and background predictions in the VBF signal region. The dashed line shows the VBF signal scaled by a factor of 30. The hatched band shows the sum in quadrature of statistical and systematic uncertainties of the signal and background predictions taking into account the pulls and data-constraints of the nuisance parameters, and the correlations between the fit regions.

theoretical predictions of some of the background processes to data. CRs are defined for the main background processes: WW (only for $N_{\text{jet}} \leq 1$ final states), top-quark, and $Z \to \tau\tau$. For the $N_{\text{jet}} = 0$ and $N_{\text{jet}} = 1$ WW CRs, the $m_{\ell\ell}$ cut is inverted with respect to the SRs. For the top-quark CRs, the b-veto is replaced with a b-tag requirement. For the $N_{\text{jet}} = 1$ and $N_{\text{jet}} \geq 2$ $Z \to \tau\tau$ CRs, the $m_{\tau\tau}$ selection is inverted while for the $N_{\text{jet}} = 0$ $Z \to \tau\tau$ CR the $\Delta\phi_{\ell\ell}$ selection criterium is inverted. Table 3 summarises the event selection for all CRs.

Table 3: Event selection criteria used to define the control regions. Every control region selection starts from the selection labeled "Preselection" in Table 2. $N_{b\text{-jet},(20\,\text{GeV}<p_\text{T}<30\,\text{GeV})}$ represents the number of b-jet with $20\,\text{GeV} < p_\text{T} < 30\,\text{GeV}$ and $|\eta| < 2.5$.

CR	$N_{\text{jet}} = 0$	$N_{\text{jet}} = 1$	$N_{\text{jet}} \geq 2$, VBF
WW	$55 < m_{\ell\ell} < 110$ GeV $\Delta\phi_{\ell\ell} < 2.6$	$m_{\ell\ell} > 80$ GeV $\|m_{\tau\tau} - m_Z\| > 25$ GeV b-jet veto $m_\text{T}^\ell > 50$ GeV	
Top-quark	$N_{b\text{-jet},(20\,\text{GeV}<p_\text{T}<30\,\text{GeV})} > 0$ $\Delta\phi(\ell\ell, E_\text{T}^{\text{miss}}) > \pi/2$ $p_\text{T}^{\ell\ell} > 30$ GeV $\Delta\phi_{\ell\ell} < 2.8$	$N_{b\text{-jet},(p_\text{T}>30\,\text{GeV})} = 1$ $N_{b\text{-jet},(20\,\text{GeV}<p_\text{T}<30\,\text{GeV})} = 0$ $\max\left(m_\text{T}^\ell\right) > 50$ GeV $m_{\tau\tau} < m_Z - 25$ GeV	$N_{b\text{-jet},(p_\text{T}>20\,\text{GeV})} = 1$ Central Jet Veto Outside Lepton Veto
$Z \to \tau\tau$	no $E_\text{T}^{\text{miss, track}}$ requirement $m_{\ell\ell} < 80$ GeV $\Delta\phi_{\ell\ell} > 2.8$	$m_{\tau\tau} > m_Z - 25$ GeV	Outside Lepton Veto Central Jet Veto $N_{b\text{-jet},(p_\text{T}>20\,\text{GeV})} = 0$

The background contributions with misidentified leptons are estimated using a data-driven technique. A control sample where one of the two lepton candidates fails to meet the nominal identification and isolation criteria but satisfies looser identification criteria, denoted as anti-identified lepton, is used. The

contribution of this background in the SRs and CRs is then obtained by scaling the number of the events in the control samples by an extrapolation factor. The latter is measured in a Z+jets-enriched data sample, where the Z boson decays to a pair of electrons or muons, and the misidentified lepton candidate is recoiling against the Z boson. The factor is defined as the ratio of the well-identified leptons over the anti-identified ones and it is measured in bins of p_T and η. The total uncertainty on the background with misidentified leptons includes uncertainties due to the difference in the sample composition between W+jets and Z+jets control samples determined with MC simulation, the statistical uncertainty on the Z+jets control sample, and the subtraction of other processes. In the VBF regions, the background with one misidentified lepton estimation is corrected for the contamination of events with two misidentified leptons, whose origin are largely QCD multi-jet events. This contribution is negligible in other regions. Details of this method can be found in Ref. [56].

The ggF and VBF cross-sections are obtained from a statistical analysis of the data samples by maximising a likelihood function (fit) using scaling parameters multiplying the predicted total production cross-section of each signal process using the profile likelihood method. The CRs are used to determine the normalisation of the corresponding backgrounds. For both the $N_{jet} = 0$ and $N_{jet} = 1$ ggF SR, eight fit regions are defined by subdividing in $m_{\ell\ell}$ at $m_{\ell\ell} < 30$ GeV and $m_{\ell\ell} \geq 30$ GeV, in p_T of the sub-leading lepton at $p_T^{sublead} < 20$ GeV and $p_T^{sublead} \geq 20$ GeV, and by the flavour of the subleading lepton. The discriminant variable m_T is used in all of the ggF fit regions with eight bins for the $N_{jet} = 0$ and six bins for the $N_{jet} = 1$ regions. The bin boundaries are chosen such that approximately the same number of signal events is expected in each bin for a given m_T distribution. For the $N_{jet} \geq 2$ VBF SR, the BDT score is used as discriminant variable with four bins. The signal purity increases with increasing value of the BDT score. The bin boundaries are chosen to maximise the expected sensitivity for measuring the VBF production mode, resulting in smaller bin widths for larger values of the BDT score. In the last BDT bin the signal over background ratio is about 0.6. The ggF and VBF cross-sections are determined by performing a combined simultaneous fit with all ggF fit regions, the VBF SR, and the ggF and VBF CRs. The systematic uncertainties enter the fit as nuisance parameters in the likelihood function and their correlations are taken into account. All results presented in this note are extracted from this simultaneous combined fit. Other production and decay modes of the Higgs boson are either fixed to SM prediction (VH production and $H \to \tau\tau$ decay) or neglected ($t\bar{t}H$ production).

The m_T distributions for the $N_{jet} = 0$ and $N_{jet} = 1$ SRs are shown in Figure 2. The BDT distribution for the VBF enriched region is presented in Figure 3. Table 4 shows the post-fit yields for all of the three signal regions.

The sources of uncertainty can be classified into two categories: experimental and theoretical. The dominant experimental uncertainties are the jet energy scale and resolution [57], and the b-tagging efficiency [52]. Other sources of uncertainty are lepton energy (momentum) scale and resolution, identification and isolation criteria [45, 58, 59], missing transverse momentum estimation [53], modeling of pile-up, and luminosity measurement [60]. The luminosity uncertainty is only applied to background processes which are normalised to the theory prediction and to the signal processes. For the main processes, the theoretical uncertainties are assessed by a comparison between nominal and alternative event generators and parton shower model, as indicated in Table 1. For the prediction of other VV production, variations of the matching scale are considered instead of an alternative generator. In addition, variations of the factorization and renormalization QCD scales, and the PDF model uncertainties are evaluated. The theory uncertainties on the non-resonant WW background represents one of the largest uncertainties of the order of 5% on the measured ggF cross-section. The uncertainties on the ratio of $gg \to WW$ over $qq \to WW$ comes from limited NLO accuracy of the $gg \to WW$ production cross-section [36].

(a) $N_{jet} = 0$ (b) $N_{jet} = 1$

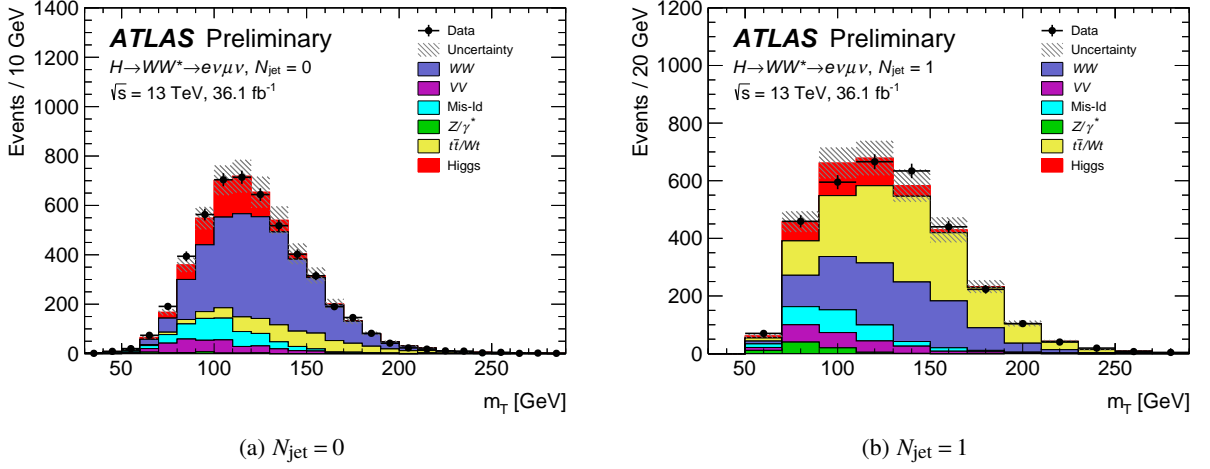Figure 2: Post-fit m_T distributions with signal and background predictions in the $N_{jet} = 0$ and $N_{jet} = 1$ signal regions. The SM Higgs boson signal prediction shown is summed over all production processes. The hatched band shows the sum in quadrature of statistical and systematic uncertainties of the signal and background predictions taking into account the pulls and data-constraints of the nuisance parameters, and the correlations between the fit regions.
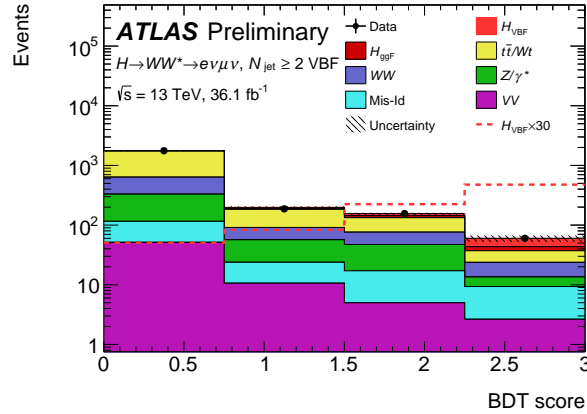

Figure 3: Post-fit BDT score distribution with the signal and the background predictions in the VBF SR. The dashed line shows the expected VBF signal scaled by a factor of 30. The hatched band shows the sum in quadrature of statistical and systematic uncertainties of the signal and background predictions taking into account the pulls and data-constraints of the nuisance parameters, and the correlations between the fit regions.

The uncertainty on the cross-section with similar acceptance cuts to this analysis has been evaluated in Ref. [61] for $N_{jet} = 0$ and $N_{jet} = 1$, respectively. The QCD scale uncertainties of the ggF contamination in the VBF region is one of the leading uncertainties on the measured VBF cross-section of the order of 15%. The uncertainty due to limited MC statistics also has a relatively large impact, especially for the VBF cross-section measurement where it contributes 23%. Table 5 shows the relative impact of the main uncertainties on the measured value of the σ_{ggF} and σ_{VBF}.

Figure 4 shows the combined m_T distribution for $N_{jet} \leq 1$. The bottom pad of Figure 4 shows the residuals of the data with respect to the total estimated background compared to the observed m_T distribution of a SM Higgs boson with $m_H = 125$ GeV. Good modelling of the residuals is observed.

Table 4: Post-fit MC and data yields in ggF and VBF SRs. The yields and the uncertainties take into account the pulls and data-constraints of the nuisance parameters, and the correlations between the fit regions and the background processes. The quoted uncertainties include the theoretical and experimental systematic sources and those due to sample statistics. The sum of all the contributions may differ from the total value due to rounding. In the determination of the uncertainties on the total background correlations have been taken into account.

Process	$N_{\text{jet}} = 0$ SR		$N_{\text{jet}} = 1$ SR		$N_{\text{jet}} \geq 2$ VBF SR
ggF	680	± 110	303	$\pm$ 52	37 ± 13
VBF	6.8 $\pm$	0.8	30.0 $\pm$	1.9	30 ± 16
WW	2960	± 670	1020	± 390	386 ± 59
VV	323	$\pm$ 34	204	$\pm$ 30	71 ± 14
$t\bar{t}/Wt$	580	± 128	1400	± 180	1234 ± 89
Mis-Id	471	$\pm$ 80	246	$\pm$ 50	109 ± 38
Z/γ^*	27	$\pm$ 10	76	$\pm$ 22	298 ± 42
Total	5062	$\pm$ 67	3290	$\pm$ 51	2138 ± 47
Observed	5089		3264		2164

Table 5: Breakdown of the main contributions to the total uncertainty in σ_{ggF} and σ_{VBF}. The sum in quadrature of the individual components differs from the total uncertainty due to correlations between the components.

Source	$\frac{\Delta\sigma_{\text{ggF}}}{\sigma_{\text{ggF}}}$ [%]	$\frac{\Delta\sigma_{\text{VBF}}}{\sigma_{\text{VBF}}}$ [%]
Data statistics	± 8	± 46
CR statistics	± 8	± 9
MC statistics	± 5	± 23
Theoretical uncertainties	± 8	± 21
ggF signal	± 5	± 15
VBF signal	< 1	± 15
WW	± 5	± 12
Top-quark	± 4	± 4
Experimental uncertainties	± 9	± 8
b-tagging	± 5	± 6
Pile-up	± 5	± 2
Jet	± 3	± 4
Electron	± 3	< 1
Misidentified leptons	± 5	± 9
Luminosity	± 2	± 3
TOTAL	± 17	± 59

The signal strength parameter μ is defined as the ratio of the measured signal yield to that predicted by the SM. The measured signal strengths for the ggF and VBF production modes in the $H \to WW^*$ decay are simultaneously determined to be

$$
\begin{aligned}
\mu_{\text{ggF}} &= 1.21^{+0.12}_{-0.11}(\text{stat.})^{+0.18}_{-0.17}(\text{sys.}) = 1.21^{+0.22}_{-0.21} \\
\mu_{\text{VBF}} &= 0.62^{+0.30}_{-0.28}(\text{stat.}) \pm 0.22(\text{sys.}) = 0.62^{+0.37}_{-0.36}.
\end{aligned}
$$

In addition the $\sigma_{\text{ggF(VBF)}} \cdot \mathcal{B}_{H \to WW^*}$ for ggF and VBF are evaluated. The branching fraction $\mathcal{B}_{H \to WW^*}$
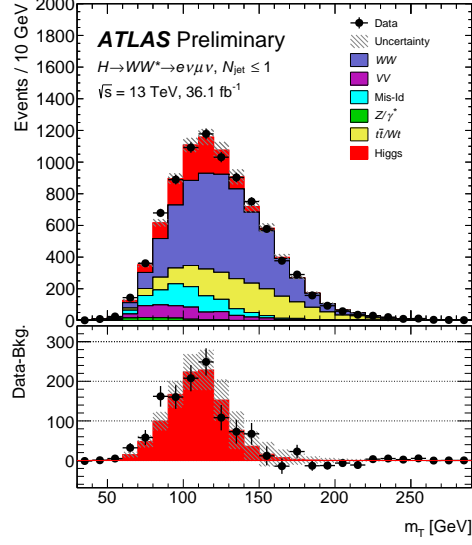
Figure 4: Post-fit combined transverse mass distribution for $N_{\text{jet}} \leq 1$. The SM Higgs boson signal prediction shown is summed over all production processes. The bottom pad shows the residuals of the data with respect to the estimated background compared to the distribution for a SM Higgs boson with $m_H = 125$ GeV. The background and signal processes are normalised to the result of the statistical analysis. The hatched band shows the sum in quadrature of statistical and systematic uncertainties of the signal and background predictions taking into account the pulls and data-constraints of the nuisance parameters, and the correlations between the fit regions.

is $0.2137 \pm 0.99\%(\text{TH})^{+0.99\%}_{-0.98\%}(\text{PU}(m_q))^{+0.66\%}_{-0.63\%}(\text{PU}(\alpha_S))$ [62]. The central value is the product of μ and the predicted SM cross-section time branching fraction. The resulting cross-sections times branching fractions are simultaneously determined to be

$$
\begin{aligned}
\sigma_{\text{ggF}} \cdot \mathcal{B}_{H \to WW^*} &= 12.6^{+1.3}_{-1.2}(\text{stat.})^{+1.9}_{-1.8}(\text{sys.}) \text{ pb} = 12.6^{+2.3}_{-2.1} \text{ pb} \\
\sigma_{\text{VBF}} \cdot \mathcal{B}_{H \to WW^*} &= 0.50^{+0.24}_{-0.23}(\text{stat.}) \pm 0.18(\text{sys.}) \text{ pb} = 0.50^{+0.30}_{-0.29} \text{ pb}.
\end{aligned}
$$

The predicted cross-section times branching fraction values are 10.4 ± 0.6 pb and 0.81 ± 0.02 pb for ggF and VBF [62], respectively. The observed (expected) significances of ggF and VBF productions are 6.3 (5.2) standard deviations and 1.9 (2.7) standard deviations, respectively. When determining the significance for the VBF production, the ggF production is profiled, and vice-versa. The 68% and 95% confidence level two-dimensional contours of $\sigma_{\text{ggF}} \cdot \mathcal{B}_{H \to WW^*}$ and $\sigma_{\text{VBF}} \cdot \mathcal{B}_{H \to WW^*}$ are shown in Figure 5.

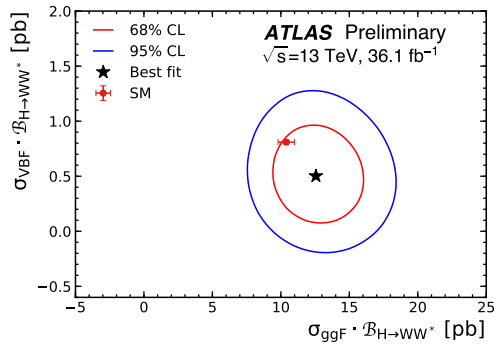The measurement of the ggF and VBF cross-sections are in agreement with the SM predictions within 1σ.

Figure 5: 68% and 95% confidence level two-dimensional likelihood contours of $\sigma_{\mathrm{ggF}} \cdot \mathcal{B}_{H \to WW^*}$ vs. $\sigma_{\mathrm{VBF}} \cdot \mathcal{B}_{H \to WW^*}$, compared to the Standard Model prediction (red cross).

References

[1] ATLAS Collaboration, *The ATLAS Experiment at the CERN Large Hadron Collider*,
JINST **3** (2008) S08003.

[2] ATLAS Collaboration, *ATLAS Insertable B-Layer Technical Design Report Addendum*,
tech. rep. CERN-LHCC-2012-009. ATLAS-TDR-19-ADD-1,
Addendum to CERN-LHCC-2010-013, ATLAS-TDR-019, 2012,
URL: https://cds.cern.ch/record/1451888.

[3] ATLAS Collaboration, *Performance of the ATLAS Trigger System in 2015*,
Eur. Phys. J. **C77** (2017) 317, arXiv: 1611.09661 [hep-ex].

[4] P. Nason and C. Oleari,
NLO Higgs boson production via vector-boson fusion matched with shower in POWHEG,
JHEP **02** (2010) 037, arXiv: 0911.5299 [hep-ph].

[5] K. Hamilton, P. Nason, E. Re and G. Zanderighi, *NNLOPS simulation of Higgs boson production*,
JHEP **10** (2013) 222, arXiv: 1309.0017 [hep-ph].

[6] J. M. Campbell et al., *NLO Higgs Boson Production Plus One and Two Jets Using the POWHEG
BOX, MadGraph4 and MCFM*, JHEP **07** (2012) 092, arXiv: 1202.5475 [hep-ph].

[7] J. Butterworth et al., *PDF4LHC recommendations for LHC Run II*, J. Phys. **G43** (2016) 023001,
arXiv: 1510.03865 [hep-ph].

[8] T. Sjostrand, S. Mrenna and P. Z. Skands, *A Brief Introduction to PYTHIA 8.1*,
Comput. Phys. Commun. **178** (2008) 852, arXiv: 0710.3820 [hep-ph].

[9] ATLAS Collaboration, *Measurement of the Z/γ^* boson transverse momentum distribution in pp
collisions at $\sqrt{s} = 7$ TeV with the ATLAS detector*, JHEP **09** (2014) 145,
arXiv: 1406.3660 [hep-ex].

[10] LHC Higgs Cross Section Working Group, *Handbook of LHC Higgs Cross Sections: 3. Higgs
Properties: Report of the LHC Higgs Cross Section Working Group*,
tech. rep. CERN-2013-004. CERN-2013-004, 2013,
URL: https://cds.cern.ch/record/1559921.

[11] C. Anastasiou, C. Duhr, F. Dulat, F. Herzog and B. Mistlberger,
Higgs Boson Gluon-Fusion Production in QCD at Three Loops,
Phys. Rev. Lett. **114** (2015) 212001, arXiv: 1503.06056 [hep-ph].

[12] C. Anastasiou et al.,
High precision determination of the gluon fusion Higgs boson cross-section at the LHC,
JHEP **05** (2016) 058, arXiv: 1602.00695 [hep-ph].

[13] S. Actis, G. Passarino, C. Sturm and S. Uccirati,
NLO Electroweak Corrections to Higgs Boson Production at Hadron Colliders,
Phys. Lett. **B670** (2008) 12, arXiv: 0809.1301 [hep-ph].

[14] C. Anastasiou, R. Boughezal and F. Petriello,
Mixed QCD-electroweak corrections to Higgs boson production in gluon fusion,
JHEP **04** (2009) 003, arXiv: 0811.3458 [hep-ph].

[15] M. Ciccolini, A. Denner and S. Dittmaier, *Strong and electroweak corrections to the production of
Higgs boson + 2 jets via weak interactions at the LHC*, Phys. Rev. Lett. **99** (2007) 161803,
arXiv: 0707.0381 [hep-ph].

[16] M. Ciccolini, A. Denner and S. Dittmaier,
Electroweak and QCD corrections to Higgs production via vector-boson fusion at the LHC,
Phys. Rev. **D77** (2008) 013002, arXiv: 0710.4749 [hep-ph].

[17] P. Bolzoni, F. Maltoni, S.-O. Moch and M. Zaro,
Higgs production via vector-boson fusion at NNLO in QCD, Phys. Rev. Lett. **105** (2010) 011801,
arXiv: 1003.4451 [hep-ph].

[18] S. Agostinelli et al., *GEANT4: A simulation toolkit*, Nucl. Instrum. Meth. A **506** (2003) 250.

[19] ATLAS Collaboration, *The ATLAS Simulation Infrastructure*, Eur. Phys. J. **C70** (2010) 823,
arXiv: 1005.4568 [physics.ins-det].

[20] ATLAS Collaboration, *Summary of ATLAS Pythia 8 tunes*, ATL-PHYS-PUB-2012-003, 2012,
URL: https://cds.cern.ch/record/1474107.

[21] A. D. Martin, W. J. Stirling, R. S. Thorne and G. Watt, *Parton distributions for the LHC*,
Eur. Phys. J. **C63** (2009) 189, arXiv: 0901.0002 [hep-ph].

[22] J. Alwall et al., *The automated computation of tree-level and next-to-leading order differential
cross sections, and their matching to parton shower simulations*, JHEP **07** (2014) 079,
arXiv: 1405.0301 [hep-ph].

[23] R. Frederix and S. Frixione, *Merging meets matching in MC@NLO*, JHEP **12** (2012) 061,
arXiv: 1209.6215 [hep-ph].

[24] J. Bellm et al., *Herwig 7.0/Herwig++ 3.0 release note*, Eur. Phys. J. **C76** (2016) 196,
arXiv: 1512.01178 [hep-ph].

[25] G. Luisoni, P. Nason, C. Oleari and F. Tramontano, *HW±/HZ + 0 and 1 jet at NLO with the
POWHEG BOX interfaced to GoSam and their merging within MiNLO*, JHEP **10** (2013) 083,
arXiv: 1306.2542 [hep-ph].

[26] T. Han and S. Willenbrock, *QCD correction to the pp → WH and ZH total cross-sections*,
Phys. Lett. **B273** (1991).

[27] O. Brein, A. Djouadi and R. Harlander,
NNLO QCD corrections to the Higgs-strahlung processes at hadron colliders,
Phys. Lett. **B579** (2004) 149, arXiv: hep-ph/0307206 [hep-ph].

[28] M. Ciccolini, S. Dittmaier and M. Krmer,
Electroweak radiative corrections to associated WH and ZH production at hadron colliders,
Phys. Rev. **D68** (2003), arXiv: 0306234 [hep-ph].

[29] T. Gleisberg et al., *Event generation with SHERPA 1.1*, JHEP **02** (2009) 007,
arXiv: 0811.4622 [hep-ph].

[30] T. Gleisberg and S. Höche, *Comix, a new matrix element generator*, JHEP **12** (2008) 039,
arXiv: 0808.3674 [hep-ph].

[31] R. D. Ball et al., *Parton distributions for the LHC Run II*, JHEP **04** (2015) 040,
arXiv: 1410.8849 [hep-ph].

[32] S. Schumann and F. Krauss,
A Parton shower algorithm based on Catani-Seymour dipole factorisation, JHEP **03** (2008) 038,
arXiv: 0709.1027 [hep-ph].

[33] S. Höche, F. Krauss, M. Schönherr and F. Siegert,
QCD matrix elements + parton showers: The NLO case, JHEP **04** (2013) 027,
arXiv: 1207.5030 [hep-ph].

[34] F. Cascioli et al., *Precise Higgs-background predictions: merging NLO QCD and squared quark-loop corrections to four-lepton + 0,1 jet production*, JHEP **01** (2014) 046,
arXiv: 1309.0500 [hep-ph].

[35] H.-L. Lai et al., *New parton distributions for collider physics*, Phys. Rev. **D82** (2010) 074024,
arXiv: 1007.2241 [hep-ph].

[36] F. Caola, K. Melnikov, R. Röntsch and L. Tancredi,
QCD corrections to W^+W^- production through gluon fusion, Phys. Lett. **B754** (2016) 275,
arXiv: 1511.08617 [hep-ph].

[37] S. Höche, S. Schumann and F. Siegert,
Hard photon production and matrix-element parton-shower merging,
Phys. Rev. **D81** (2010) 034026, arXiv: 0912.3501 [hep-ph].

[38] S. Frixione, P. Nason and G. Ridolfi,
A Positive-weight next-to-leading-order Monte Carlo for heavy flavour hadroproduction,
JHEP **09** (2007) 126, arXiv: 0707.3088 [hep-ph].

[39] T. Sjostrand, S. Mrenna and P. Z. Skands, *A Brief Introduction to PYTHIA 8.1*,
Comput. Phys. Commun. **178** (2008) 852, arXiv: 0710.3820 [hep-ph].

[40] M. Czakon, P. Fiedler and A. Mitov,
Total Top-Quark Pair-Production Cross Section at Hadron Colliders Through $\alpha(\frac{4}{S})$,
Phys. Rev. Lett. **110** (2013) 252004, arXiv: 1303.6254 [hep-ph].

[41] E. Re,
Single-top Wt-channel production matched with parton showers using the POWHEG method,
Eur. Phys. J. **C71** (2011) 1547, arXiv: 1009.2450 [hep-ph].

[42] T. Sjöstrand, S. Mrenna and P. Z. Skands, *PYTHIA 6.4 Physics and Manual*, JHEP **05** (2006) 026,
arXiv: hep-ph/0603175 [hep-ph].

[43] S. Kallweit, J. M. Lindert, P. Maierhofer, S. Pozzorini and M. Schönherr, *NLO QCD+EW predictions for V + jets including off-shell vector-boson decays and multijet merging*,
JHEP **04** (2016) 021, arXiv: 1511.08692 [hep-ph].

[44] ATLAS Collaboration, *Electron efficiency measurements with the ATLAS detector using 2012 LHC proton–proton collision data*, Eur. Phys. J. C **77** (2017) 195, arXiv: 1612.01456 [hep-ex].

[45] ATLAS Collaboration, *Electron efficiency measurements with the ATLAS detector using the 2015 LHC proton–proton collision data*, ATLAS-CONF-2016-024, 2016,
URL: https://cds.cern.ch/record/2157687.

[46] ATLAS Collaboration, *Muon reconstruction performance of the ATLAS detector in proton–proton collision data at $\sqrt{s}$ = 13 TeV*, Eur. Phys. J. C **76** (2016) 292, arXiv: 1603.05598 [hep-ex].

[47] ATLAS Collaboration,
Electron identification measurements in ATLAS using $\sqrt{s}$ = 13 TeV data with 50 ns bunch spacing,
ATL-PHYS-PUB-2015-041, 2015, URL: https://cds.cern.ch/record/2048202.

[48] M. Cacciari, G. P. Salam and G. Soyez, *The Anti-k(t) jet clustering algorithm*,
JHEP **04** (2008) 063, arXiv: 0802.1189 [hep-ph].

[49] ATLAS Collaboration, *Jet energy scale measurements and their systematic uncertainties in proton–proton collisions at $\sqrt{s}$ = 13 TeV with the ATLAS detector*, Phys. Rev. D **96** (2017) 072002, arXiv: `1703.09665 [hep-ex]`.

[50] ATLAS Collaboration, *Tagging and suppression of pileup jets with the ATLAS detector*, ATLAS-CONF-2014-018, 2014, URL: `https://cds.cern.ch/record/1700870`.

[51] ATLAS Collaboration, *Identification and rejection of pile-up jets at high pseudorapidity with the ATLAS detector*, Eur. Phys. J. **C77** (2017) 580, [Erratum: Eur. Phys. J.C77,no.10,712(2017)], arXiv: `1705.02211 [hep-ex]`.

[52] ATLAS Collaboration, *Optimisation of the ATLAS b-tagging performance for the 2016 LHC Run*, ATL-PHYS-PUB-2016-012, 2016, URL: `https://cds.cern.ch/record/2160731`.

[53] ATLAS Collaboration, *Performance of missing transverse momentum reconstruction with the ATLAS detector in the first proton–proton collisions at $\sqrt{s}$ = 13 TeV*, ATL-PHYS-PUB-2015-027, 2015, URL: `https://cds.cern.ch/record/2037904`.

[54] T. Plehn, D. L. Rainwater and D. Zeppenfeld, *A Method for identifying $H \rightarrow \tau^+\tau^- \rightarrow e^\pm \mu^\mp p_T$ at the CERN LHC*, Phys. Rev. **D61** (2000) 093005, arXiv: `hep-ph/9911385 [hep-ph]`.

[55] J. H. Friedman, *Greedy function approximation: A gradient boosting machine.*, Ann. Statist. **29** (2001) 1189.

[56] ATLAS Collaboration, *Observation and measurement of Higgs boson decays to WW^* with the ATLAS detector*, Phys. Rev. **D92** (2015) 012006, arXiv: `1412.2641 [hep-ex]`.

[57] ATLAS Collaboration, *Jet Calibration and Systematic Uncertainties for Jets Reconstructed in the ATLAS Detector at $\sqrt{s}$ = 13 TeV*, ATL-PHYS-PUB-2015-015, 2015, URL: `https://cds.cern.ch/record/2037613`.

[58] ATLAS Collaboration, *Electron and photon energy calibration with the ATLAS detector using data collected in 2015 at $\sqrt{s}$ = 13 TeV*, ATL-PHYS-PUB-2016-015, 2016, URL: `https://cds.cern.ch/record/2203514`.

[59] ATLAS Collaboration, *Muon reconstruction performance of the ATLAS detector in proton–proton collision data at $\sqrt{s}$ =13 TeV*, Eur. Phys. J. **C76** (2016) 292, arXiv: `1603.05598 [hep-ex]`.

[60] ATLAS Collaboration, *Luminosity determination in pp collisions at $\sqrt{s}$ = 8 TeV using the ATLAS detector at the LHC*, Eur. Phys. J. **C76** (2016) 653, arXiv: `1608.03953 [hep-ex]`.

[61] T. Melia, K. Melnikov, R. Rontsch, M. Schulze and G. Zanderighi, *Gluon fusion contribution to W^+W^- + jet production*, JHEP **08** (2012) 115, arXiv: `1205.6987 [hep-ph]`.

[62] LHC Higgs Cross Section Working Group, *Handbook of LHC Higgs Cross Sections: 4. Deciphering the Nature of the Higgs Sector*, (2016), arXiv: `1610.07922 [hep-ph]`.

Appendix

This Appendix includes a collection of supplementary figures and tabulated information. Table 6 lists the expected signal and background contributions to the Control Regions and the observed yields in the data. Table 7 lists the expected signal and background contributions for each bin in the BDT output for the VBF SR and the observed yields in the data. Figure 6 shows the $m_{\ell\ell}$ and p_T^{sublead} distributions in the $N_{\text{jet}} = 0$ and $N_{\text{jet}} = 1$ SRs. Figure 7 show the m_T distributions in the $N_{\text{jet}} = 0$ and $N_{\text{jet}} = 1$ CRs for the WW, top-quark and $Z \to \tau\tau$ processes. Figure 8 shows the $m_{\ell\ell}$ and $\Delta\phi_{\ell\ell}$ distributions in the VBF SR. Finally, Figure 9 shows the Δy_{jj} distributions in the $N_{\text{jet}} \ge 2$ top-quark and $Z \to \tau\tau$ CRs.

Table 6: Post-fit MC and data yields for the ggF and VBF analysis in the CRs. The yields and the uncertainties take into account the pulls and data-constraints of the nuisance parameters, and the correlations between the fit regions and the background processes. The quoted uncertainties include the theoretical and experimental systematic sources and those due to sample statistics. The sum of all the contributions may differ from the total value due to rounding. In the determination of the uncertainties on the total background correlations have been taken into account.

Process	Higgs		WW		VV		$t\bar{t}/Wt$		Z/γ^*		Mis-Id		Total	Observed
$N_{\text{jet}} = 0$ WW CR	124	± 19	4870	± 340	311	± 34	1180	± 240	355	± 51	630	± 130	7467 ± 84	7461
$N_{\text{jet}} = 0$ Top-quark CR	24.8	± 4.4	240	± 44	33.0	± 7.7	2956	± 89	47	± 16	95	± 23	3396 ± 60	3399
$N_{\text{jet}} = 0$ Z+jets CR	160	± 10	894	± 64	941	± 77	70	± 17	40 880	± 670	2510	± 650	$45\,460 \pm 220$	45463
$N_{\text{jet}} = 1$ WW CR	13.59	± 0.66	3540	± 800	343	± 60	5170	± 730	200	± 50	500	± 120	9770 ± 100	9784
$N_{\text{jet}} = 1$ Top-quark CR	29.4	± 5.0	213	± 56	31.5	± 6.3	18 740	± 180	76	± 14	345	± 87	$19\,430 \pm 150$	19428
$N_{\text{jet}} = 1$ Z+jets CR	71.1	± 5.4	290	± 67	142	± 21	302	± 38	2526	± 87	238	± 61	3571 ± 62	3571
$N_{\text{jet}} \ge 2$ VBF Top-quark CR	8.1	± 1.5	51.8	± 6.4	9.9	± 4.6	7381	± 96	47.2	± 8.4	162	± 36	7660 ± 87	7668
$N_{\text{jet}} \ge 2$ VBF Z+jets CR	9.1	± 0.9	21.2	± 2.8	20.5	± 5.2	57.7	± 6.0	364	± 25	24.9	± 2.6	497 ± 22	501

Table 7: Post-fit MC and data yields in each BDT bin for the VBF SR. The yields and the uncertainties take into account the pulls and data-constraints of the nuisance parameters, and the correlations between the fit regions and the background processes. The quoted uncertainties include the theoretical and experimental systematic sources and those due to sample statistics. The sum of all the contributions may differ from the total value due to rounding. In the determination of the uncertainties on the total background correlations have been taken into account.

Process	Bin1	Bin2	Bin3	Bin4
VV	51.4 ± 7.2	10.6 ± 3.3	5.0 ± 2.3	2.6 ± 1.6
WW	306 ± 18	34.4 ± 5.9	28.7 ± 5.4	10.2 ± 3.2
Mis-Id	64.1 ± 8.5	13.2 ± 3.9	12.2 ± 3.7	6.7 ± 2.7
Z/γ^*	214 ± 15	33.0 ± 5.9	30.1 ± 5.6	4.2 ± 2.1
$t\bar{t}/Wt$	1102 ± 33	92.7 ± 9.6	56.7 ± 7.4	13.4 ± 3.7
H_{ggF}	17.3 ± 3.8	10.2 ± 2.9	11.2 ± 3.0	6.4 ± 2.3
Total	1760 ± 42	195 ± 14	145 ± 12	43.8 ± 6.6
H_{VBF}	1.7 ± 1.4	2.8 ± 1.7	7.5 ± 2.8	15.9 ± 4.1
Data	1761	187	156	60

(a) $N_{\text{jet}} = 0 \; m_{\ell\ell}$

(b) $N_{\text{jet}} = 0 \; p_{\text{T}}^{\text{sublead}}$

(c) $N_{\text{jet}} = 1 \; m_{\ell\ell}$
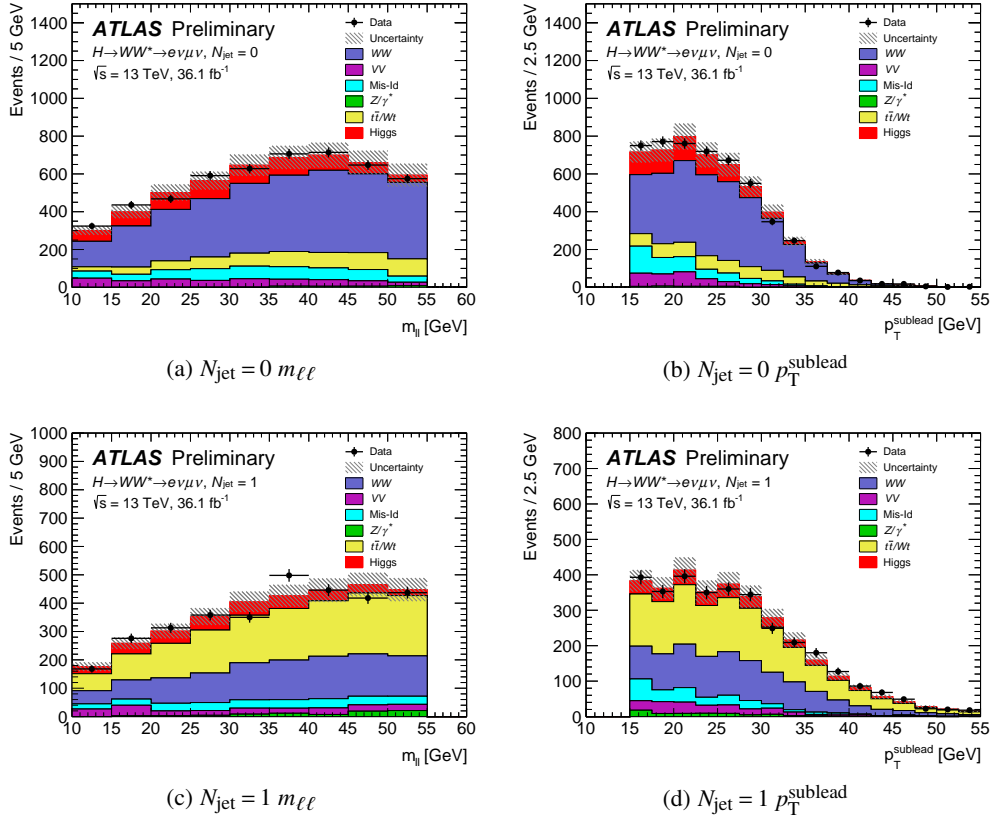
(d) $N_{\text{jet}} = 1 \; p_{\text{T}}^{\text{sublead}}$

Figure 6: Post-fit $m_{\ell\ell}$ and $p_{\text{T}}^{\text{sublead}}$ distributions with signal and background predictions in the $N_{\text{jet}} = 0$ and $N_{\text{jet}} = 1$ signal regions. The SM Higgs boson signal prediction shown is summed over all production processes. The hatched band shows the sum in quadrature of statistical and systematic uncertainties of the predictions taking into account the pulls and data-constraints of the nuisance parameters, and the correlations between the fit regions. The shape of the $p_{\text{T}}^{\text{sublead}}$ distribution can be explained by the different thresholds of the electron and muon (di-)lepton triggers.
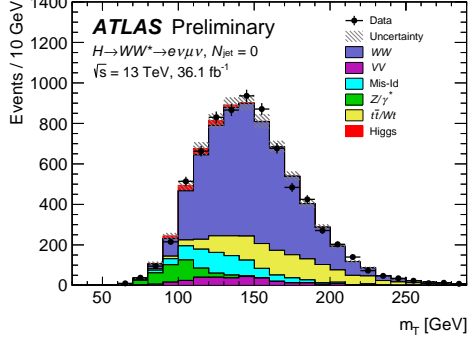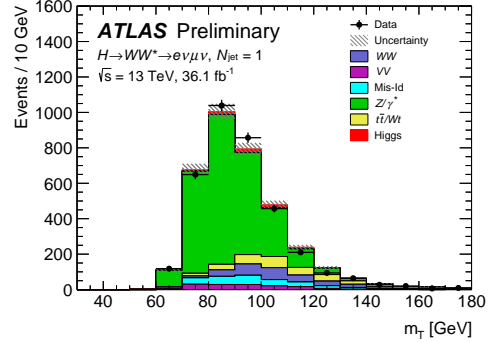
(a) $N_{jet} = 0$ WW CR
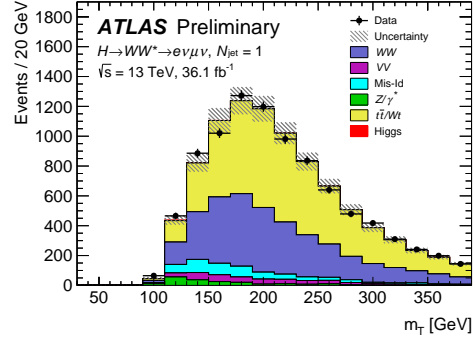
(b) $N_{jet} = 1$ WW CR
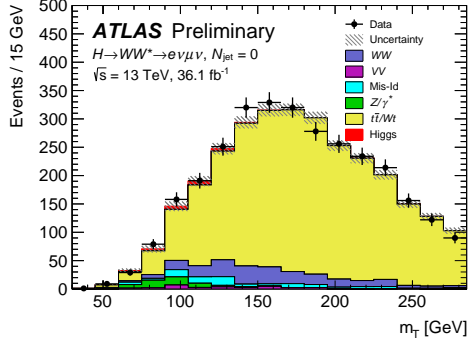
(c) $N_{jet} = 0$ top-quark CR
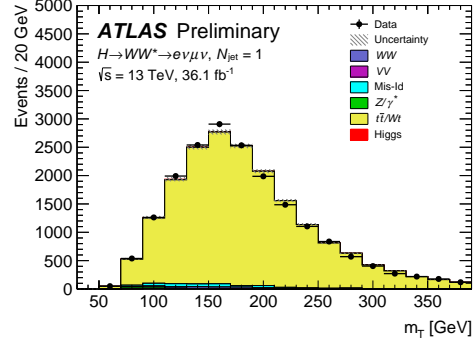
(d) $N_{jet} = 1$ top-quark CR
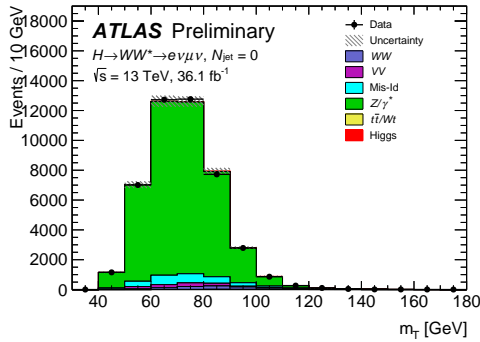
(e) $N_{jet} = 0$ $Z \to \tau\tau$ CR

(f) $N_{jet} = 1$ $Z \to \tau\tau$ CR

Figure 7: Post-fit m_T distributions with signal and background expectations in the $N_{jet} = 0$ and $N_{jet} = 1$ control regions for the WW, top-quark, and $Z \to \tau\tau$ processes. The SM Higgs boson signal prediction shown is summed over all production processes. The hatched band shows the sum in quadrature of statistical and systematic uncertainties of the predictions taking into account the pulls and data-constraints of the nuisance parameters, and the correlations between the fit regions.
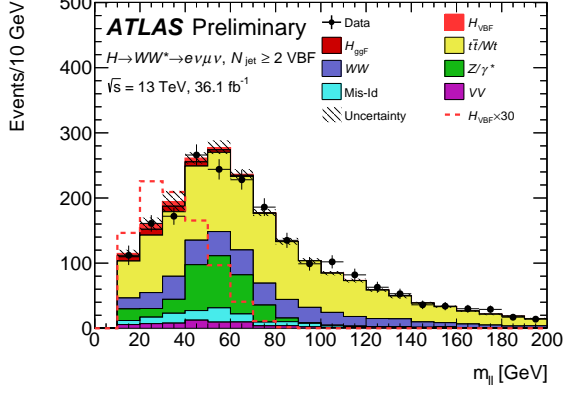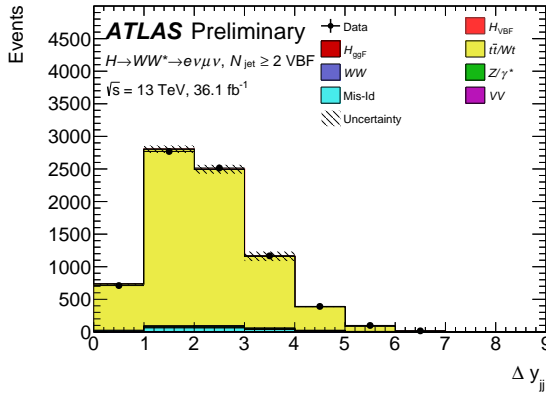
(a) $N_{\text{jet}} \geq 2$ VBF SR: $m_{\ell\ell}$
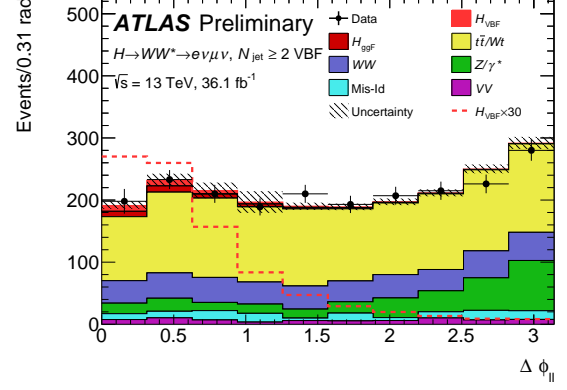
(b) $N_{\text{jet}} \geq 2$ VBF SR: $\Delta\phi_{\ell\ell}$

Figure 8: Post-fit $m_{\ell\ell}$ and $\Delta\phi_{\ell\ell}$ distributions with signal and background predictions in the VBF signal region. The dashed line shows the VBF signal scaled by a factor of 30. The hatched band shows the sum in quadrature of statistical and systematic uncertainties of the predictions taking into account the pulls and data-constraints of the nuisance parameters, and the correlations between the fit regions.

(a) $N_{\text{jet}} \geq 2$ VBF Top-quark CR
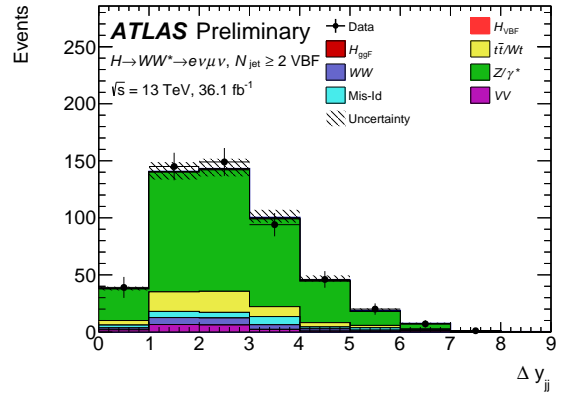
(b) $N_{\text{jet}} \geq 2$ VBF $Z \to \tau\tau$ CR

Figure 9: Post-fit Δy_{jj} distribution with signal and background predictions in the VBF top-quark and $Z \to \tau\tau$ control regions. The hatched band shows the sum in quadrature of statistical and systematic uncertainties of the predictions taking into account the pulls and data-constraints of the nuisance parameters, and the correlations between the fit regions.